Materials Today Physics 23 (2022) 100623

Contents lists available at ScienceDirect

Materials Today Physics

journal homepage: https://www.journals.elsevier.com/materials-today-physics

Unique multiferroics with tunable ferroelastic transition in antiferromagnet $Mn_2V_2O_7$

H.J. Chen [a], C.H. Yeh [a], T.W. Kuo [a], D. Chandrasekhar Kakarla [a, **], H.C. Wu [a], T.W. Yen [a], S.M. Huang [a], H. Chou [a], M.C. Chou [b, c], H.W. Chen [c], S.W. Kuo [c], Y.C. Chuang [d], C.K. Chang [d], U. Eckstein [e], N.H. Khansur [e], K.G. Webber [e], H.D. Yang [a, b, *]

[a] Department of Physics, National Sun Yat-sen University, Kaohsiung, 804, Taiwan
[b] Center of Crystal Research, National Sun Yat-sen University, Kaohsiung, 804, Taiwan
[c] Department of Materials and Optoelectronic Science, National Sun Yat-sen University, Kaohsiung, 804, Taiwan
[d] National Synchrotron Radiation Research Center, Hsinchu, 30076, Taiwan
[e] Department of Materials Science and Engineering, Friedrich-Alexander-Universität Erlangen-Nürnberg, Martensstr. 5, 91058, Erlangen, Germany

ARTICLE INFO

Article history:
Received 12 December 2021
Received in revised form
18 January 2022
Accepted 26 January 2022
Available online 7 February 2022

Keywords:
Multiferroics
Ferroelastic
Antiferromagnetic
Magnetoelastic coupling
Honeycomb-structure $Mn_2V_2O_7$

ABSTRACT

Multiferroics have received considerable interest over the last decade due to the fascinating fundamental phenomena and potential use in various applications, such as low-power electronics and spintronics. Among those, investigations have focused on the coexistence of ferroelectric and ferromagnetic materials. Here, we report the rare case that the para-to ferroelastic ordering transition in antiferromagnet $Mn_2V_2O_7$ occurred at $T_S = 260–280$ K, verified by temperature-dependent magnetization measurements, dielectric, differential scanning calorimetry, and macroscopic strain-stress hysteresis loops. Furthermore, this transition was accompanied by a structural transition from the high-temperature *C2*/m monoclinic phase (β-phase) to a low-temperature $P\,\bar{1}$ triclinic phase (α-phase), as identified by temperature-dependent X-ray diffraction. Consequently, T_S can be successfully increased by Co- and Ni-doping and decreased by Ca-doping. Thus, the phase diagram was established for the structural stability of $(Mn_{1-x}A_x)_2V_2O_7$ (A = Co, Ni, and Ca). In addition, the physical and chemical pressure effects were applied on $(Mn_{1-x}Ca_x)_2V_2O_7$ to correlate the ferroelastic (T_S) and antiferromagnetic (T_N) orderings. Consequently, the magnetoelastic coupling was revealed, and a unique multiferroic material ($Mn_2V_2O_7$) with a ferroelastic and antiferromagnetic ordering was obtained.

1. Introduction

Multiferroics are a class of materials with the coexistence of two or more ferroics, such as ferroelectric, ferromagnetic, and ferroelastic properties [1–4], represented by a famous cartoon triangle each property was occupying a corner [5]. The cross-coupling among these three properties has been highly considered as it results in rich physics and an extra degree of flexibility to tune the properties [6–11]. Over the past decade, intense research has been focused on one side of the triangle, i.e., ferroelectric and ferromagnetic, owing to anticipated novel functional devices, such as multiferroic four-state memory, magnetoelectric sensors, and multiferroic logic gates etc [12,13]. Although many applications have been found for ferroelastic materials, such as piezoelectric sensors and mechanical switches, they have not been studied adequately [14–16]. In fact, strain-mediated coupling has been widely explored in the field of multiferroics [17,18]. Ferroelasticity is an inevitable hidden key factor to achieving strong magnetoelectric coupling; it efficiently mediates the electric and magnetic dipoles [19]. To date, the number of ferroelastic materials has been found to be considerably less than that of the ferromagnetic and ferroelectric compounds [1,19]; hence, more efforts are required to find new ferroelastic materials to realize their intriguing physics and possible practical applications.

Analogous to other ferroics, ferroelasticity exhibits hysteresis in the strain versus stress curve; a mechanical switching between at

* Corresponding author. Department of Physics, National Sun Yat-sen University, Kaohsiung, 804, Taiwan.
** Corresponding author.
E-mail addresses: chandu@g-mail.nsysu.edu.tw (D.C. Kakarla), yang@mail.nsysu.edu.tw (H.D. Yang).

https://doi.org/10.1016/j.mtphys.2022.100623
2542-5293/

least two orientation states of a crystal by external stress [19]. According to the Landau theory of free energy, lowering the point group symmetry is necessary near the ferroic phase transition, which is accompanied by the emergence of at least one new macroscopic property [20]. The famous Aizu notations classify various kinds of ferroic phase transitions based on the change in the point group near the phase transition [21]. A ferroic phase can be purely ferroelastic, such as $Pb_3(PO_4)_2$ or $BiVO_4$, or coexistence of multiple ferroic properties, such as in Mn_3O_4 (ferroelectric-ferromagnetic), $BaTiO_3$ and $Pb(Zr_{1-x}Ti_x)O_3$ (ferroelastic-ferroelectric), $BiFeO_3$ (ferroelectric-ferromagnetic-ferroelastic) [19,20,22–24]. The Ni–I boracite sample is one of the well-known triple-ferroic examples for the simultaneous coexistence of ferroelectric, ferroelastic and ferromagnetism [20]. Advances in the experimental characterization methods have also proven that many multiferroics are ferroelastic. Angle-resolved polarized Raman spectroscopy explores the ferroelastic domain texture owing to the lattice deformation caused by the Jahn-Teller effect [25]. A well-known type-I multiferroic, $BiFeO_3$, has been established as a ferroelastic using Raman spectroscopy, whereas the antiferromagnetic texture is controlled using the strain and electric fields [26,27]. Low-temperature piezoresponse force microscopy has proved the existence of ferroelectric–ferroelastic domains in the skyrmions host GaV_4S_8 sample [28].

Transition metal-vanadium oxides with the general formula $A_2V_2O_7$ (A = Mn, Cu, Co, and Ni) have garnered considerable attention owing to their variety of crystallographic structures and intriguing physical properties [29–36]. Among these phases, α-$Cu_2V_2O_7$ has been reported to be an improper multiferroic material, where orbital degrees of freedom leads to polar distortion and ferro-orbital ordering favoring antiferromagnetic ordering [33]. Moreover, an existing study suggests that both $Ni_2V_2O_7$ and $Co_2V_2O_7$ exhibit magnetic-field-induced ferroelectricity [30]. In addition, $Mn_2V_2O_7$ exhibits extraordinary physical properties owing to its geometrical spin-frustrated honeycomb structure [31,32,36]. A structural transition with T_S ~280 K, antiferromagnetic ordering, and weak magnetoelectric coupling below T_N ~17 K has already been reported [32,34,36]. In particular, the nonlinear behavior in pressure-dependent capacitance measurements indicates that the low-temperature α-phase might be ferroelastic [36]. In this study, we employed various experimental tools, such as temperature-dependent X-ray diffraction (XRD), differential scanning microscopy (DSC), dielectrics, and strain-stress hysteretic loops, to confirm the para-ferroelastic transition in $Mn_2V_2O_7$ near T_S in the range of 260–280 K. Furthermore, this T_S can be tuned by the partial substitution of Ni^{2+}, Co^{2+}, and Ca^{2+} ions at the Mn sites. In addition, the physical pressure and chemical expansion effects on T_N and T_S were used to test the magnetoelastic coupling in $Mn_2V_2O_7$.

2. Experimental methods

2.1. Sample preparation and characterization

$(Mn_{1-x}Ni_x)_2V_2O_7$, $(Mn_{1-x}Co_x)_2V_2O_7$, and $(Mn_{1-x}Ca_x)_2V_2O_7$ ($0 \leq x \leq 0.2$) polycrystalline samples were synthesized by solid-state reaction method. Homogeneous stoichiometric mixtures of high-purity MnO (99.99%, Alfa Aesar), V_2O_5 (99.99%, Alfa Aesar), NiO (99.995%, Cerac), CoO (99.995%, Alfa Aesar), and CaO (99.99%, Cerac) were pressed into pellets and heated at 600 °C for 10 days with several intermediate grindings. Temperature-dependent XRD patterns were collected in both TLS-01C2 and TPS-19A with wavelength 0.88571 Å and 0.77489 Å, respectively at National Synchrotron Radiation Research Center (NSRRC) in Hsinchu, Taiwan as well as D8 Discover X-ray diffraction system (Bruker) in National Yang Ming Chiao Tung University (NYCU), Taiwan, with the wavelength $\lambda = 1.54056$ Å (Cu $K\alpha_1$).

2.2. Magnetization, pressure effects, X-ray absorption spectroscopy, dielectric, stress-strain curves, and DSC

The DC magnetization measurements were performed in a MPMS-XL 7 (Quantum Design Magnetic Property Measurement System). A piston-cylinder-type cell designed for the MPMS-XL7 was used to perform the high-pressure DC magnetization measurement with Daphne-7373 oil used as a pressure-transmitting medium and in situ pressure was measured with a lead manometer. X-ray absorption spectra (XAS) measurements of the Mn-L-edge and O–K-edge were performed at the 20A1 beamline of NSRRC. As mentioned in Fig. S1, it was clear that Mn L-edge spectra for different doping levels match the MnO standard that indicating Mn^{2+} is stable up to doping level $x = 0.3$. Oxygen spectral features remain almost the same up to 30% Ca doping level, thus much reduces the possible effects from the variation of oxygen vacancies in the Ca-doping. Temperature-dependent dielectric constant measurements in different frequencies were conducted using the Agilent E4980A precision inductance, capacitance, and resistance (LCR) meter from 10 kHz to 1.5 MHz inside a closed-cycle system with a temperature control region from 5 to 300K. The thermal properties were determined through differential scanning calorimetry (DSC) using a TA Q-20 instrument. The samples were placed in an aluminum pan in a N_2 atmosphere with a temperature controlling rate 10 K/min from −80 °C to 450 °C. To characterize the room-temperature strain-stress loop (Fig. 2(a), uniaxial compression tests were performed (and taken in NSYSU, Taiwan) using the Shimadzu AGS-X compression machine with a capacity of 50 kN. For each sample, the applied mechanical compressive stress was up to 2.3 MPa with the loading and unloading rates 0.01 mm/min. Temperature-dependent ferroelastic measurements [Fig. 2(b)–(f) taken in FAU, Germany] with a compressive load up to 5 MPa were conducted in a screw-driven load frame (Instron 5657, 30 kN) equipped with a thermal chamber (TK 26.600.LN2, Fresenberger) capable of adjusting the temperature from −150 °C to 600 °C. Cooling was achieved through liquid nitrogen. During testing, the sample was contacted by two tungsten carbide loading dies connected to alumina cylinders that extended into the thermal chamber; additional information on the experimental arrangement can be found elsewhere [37]. The mechanical load was applied with a linear rate of 0.5 MPa/s during loading and unloading for two cycles. The applied load was controlled by a load cell and the crosshead position measured the displacement. The displacement of the instrument was calibrated to remove the effects of the measurement setup under identical loading condition.

2.3. Theoretical calculation

Regarding theoretical backgrounds on ferroelasticity and elastic properties of materials, we include “background introduction”, and “twin boundary” sections in the Supplementary Material. Interested readers may refer to them and references therein. Our main theoretical approach in this work is *ab initio* methods, which include four terms in the Hamiltonian:

$$\widehat{H}_{DFT}[n(r)] = \widehat{T}[n(r)] + E_{xc}[n(r)] + \frac{e^2}{2}\iint \frac{n(r)n(r')drdr'}{|r-r'|} + V_{ext}[n(r)],$$

where $n(r)$ is the ground state electronic density, r the spatial coordinates, $\widehat{T}$ the kinetic energy of electrons, E_{xc} the exchange-correlation potential, third term is the Hartree potential, and V_{ext}

is the external potential that describes the interaction of electrons and ions. The DFT Hamiltonian helps simulate all materials, including multi-elemental ferroelastic crystals.

We employed an *ab initio* numerical calculation of A-doped $Mn_2V_2O_7$ (A = Ni, Co, and Ca) using VASP version 6.1.2. The lattice parameters (lattice constants and angles) and atomic coordinates at 300 K (*C2/m*) and 293 K ($P\bar{1}$) were collected from the available structural data [35]. The basis sets we chose for Mn, V, and O are plane waves with an energy cutoff of 400 eV by using the Projector-Augmented Plane Wave (PAW) method. Hubbard U methods have been applied in all of our DFT calculations in this work. Manganese, vanadium, nickel, and iron belong to the transitional metal group, in which the electron correlation effect is not negligible. Therefore, Hubbard U parameter is needed to account for this electronic correlation. The values of Hubbard U for nickel, vanadium, manganese and iron are 4.2 eV, 3.25 eV, 3.9 eV, and 5.3 eV, respectively. The exchange-correlation functional adopted was GGA-PBE. We used the initial structure constructed from Ref. [36] and relaxed the cell shape, volume, and atomic position while preserving its space group symmetry to relax both its electronic and ionic structure. We chose to relax them for the twin boundaries by fixing the cell shape and size of the twin boundary (the Supplementary Material Section provides details of the twin boundary preparation) but allowed the atomic positions in the unit cell to relax freely. The twin boundary unit cell was cut half at $1/2\ \vec{c}$ to make the cell size smaller to accelerate the VASP calculations without applying considerable changes in the twin boundary structure. The unit cell size contains 260 atoms, which makes VASP calculations computationally more demanding. Nevertheless, we still realized a calculation achieving less than 10^{-5} eV of self-consistent field (SCF) energy difference, and a force difference of 10^{-3} eV/ Å before terminating the VASP calculation. The same procedure described was also applied to α-$Mn_2V_2O_7$ but with a stricter convergence requirement. These produced the strain-stress curves (as shown in Fig. 6(c)), total energy (Table 1) and elastic moduli (Supplementary Tables 1 and 2) in this work.

3. Results and discussion

3.1. Structural, magnetic, dielectric and DSC measurements of $Mn_2V_2O_7$

$Mn_2V_2O_7$ exhibits a martensitic-like thermodynamically structural phase transition (β-α) and associated dielectric and magnetic anomalies near room temperature [31,34,36,38]. However, the structural phase transition and associated properties depended on the synthesized methods; both elements used to prepare sample and heating temperature slightly affect the structural transition temperature. We rechecked the β-α structural phase transition along with the magnetic and dielectric properties of $Mn_2V_2O_7$ to achieve higher consistency, as shown in Fig. 1. Fig. 1(a) demonstrates a clear β-α structural phase transition between the cooling and heating curves in the temperature window of 260–280 K (see Fig. 3). The thermal irreversibility of magnetization and dielectric measurements is shown in Fig. 1(b) and (c). Furthermore, endothermic and exothermic peaks (shown in Fig. 1(d)) in the differential scanning calorimetric (DSC) curves during the cooling and heating processes support the β-α structural phase transition. All the above observed thermal irreversibility in the structural and associated properties reflects the possible ferroelastic ordering in $Mn_2V_2O_7$.

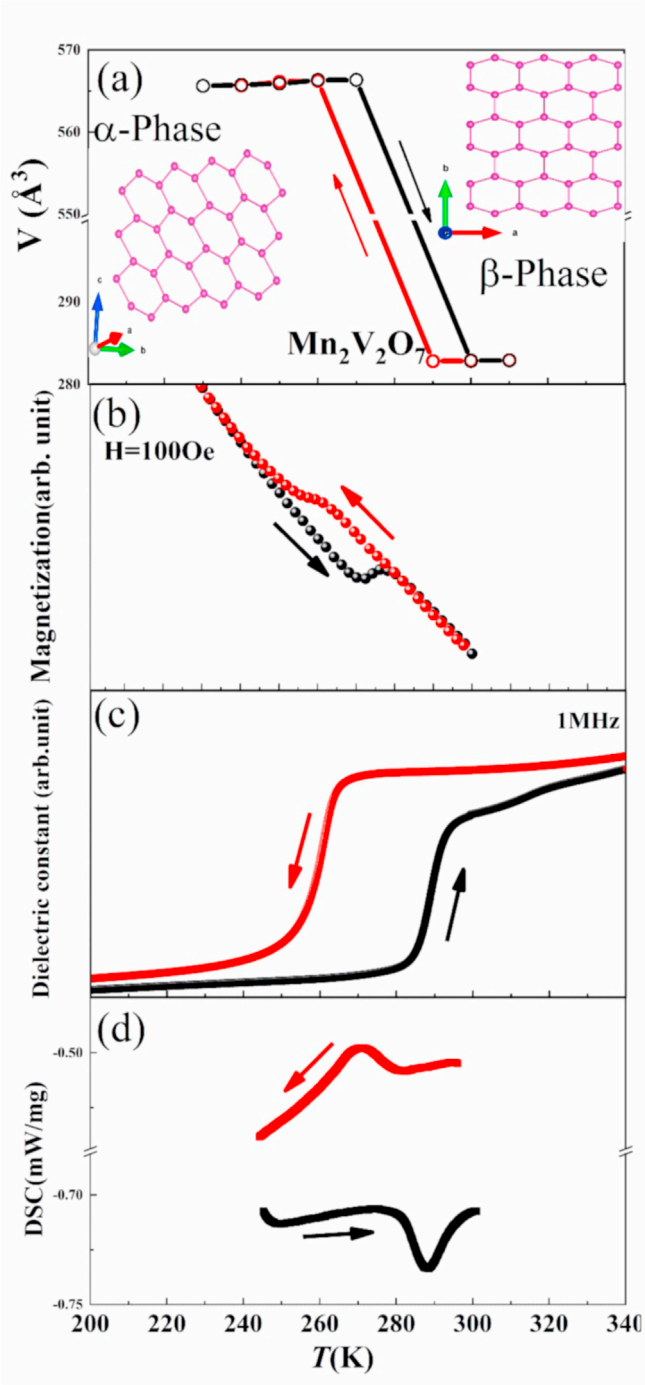

Fig. 1. Temperature-dependent (a) structural change (b) magnetization (c) dielectric and (d) DSC curves for $Mn_2V_2O_7$ during the heating and cooling cycles respectively. A clear thermal irreversibility can be noticed between the cooling and heating curves.

Table 1
The total energy obtained for the A-doped $Mn_2V_2O_7$ (A = Ni, Co, and Ca) for β and α-phase, respectively. The doping percentage of A for Mn is 10%.

A	β- $A_xMn_{2-x}V_2O_7$	α- $A_xMn_{2-x}V_2O_7$	$E(\beta)$-$E(\alpha)$ (eV)
Ni	−297.62713 eV	−298.013758 eV	0.386628
Co	−300.04754 eV	−300.116834 eV	0.069294
Ca	−302.92087 eV	−301.94751 eV	−0.97336

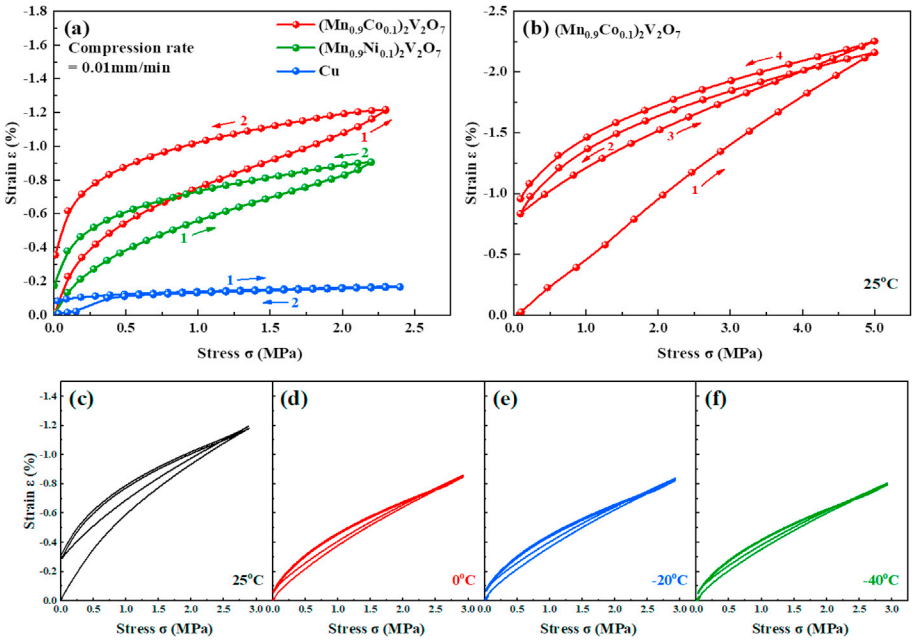

Fig. 2. (a) Room-temperature strain-stress loops (taken in National Sun Yat-sen University (NSYSU), Taiwan) for $(Mn_{0.9}A_{0.1})_2V_2O_7$ (A = Co, Ni and Ca), Cu was tested for a normal metal. Those demonstrated the loops observed in α-phase but not in β-phase. (b) Room-temperature strain-stress loops (data taken in FAU, Germany) for $(Mn_{0.9}Co_{0.1})_2V_2O_7$ sample with about double stress indicated the reproductivity in two different labs. The data measured at T = 298, 273, 253, and 233 K were shown in (c)–(f) and demonstrated the existence of ferroelastic property.

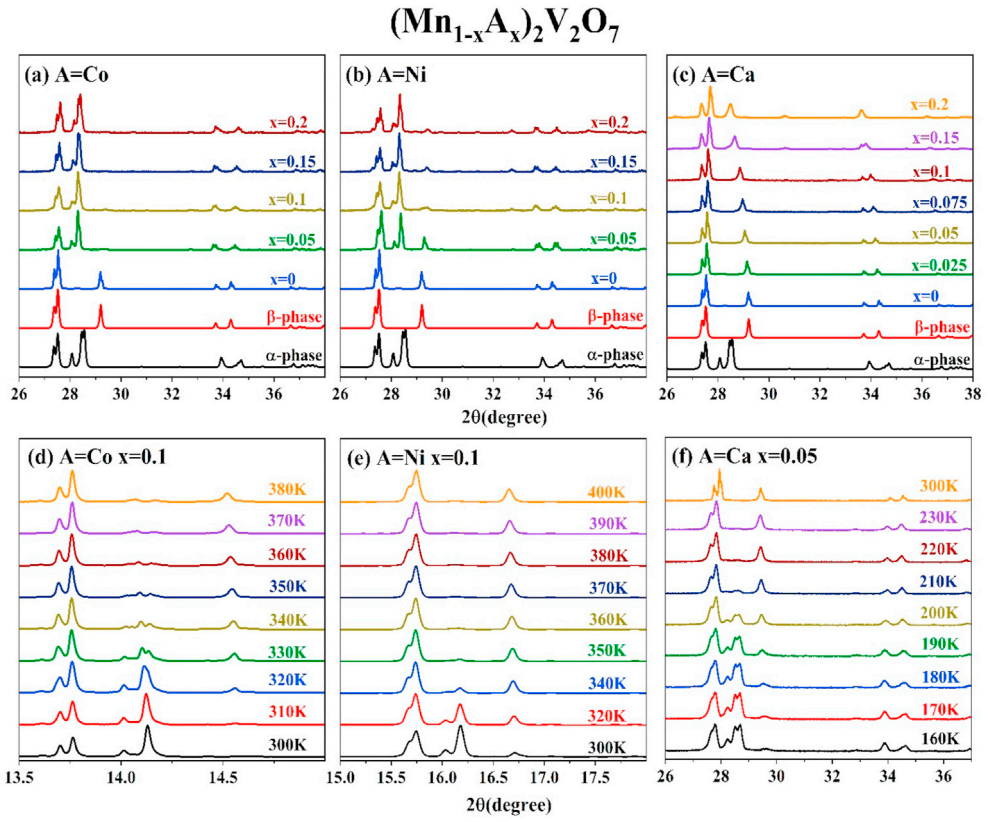

Fig. 3. Room temperature X-ray diffraction patterns for $(Mn_{1-x}A_x)_2V_2O_7$ ($0 \leq x \leq 0.20$) as well as the simulation of β and α-$Mn_2V_2O_7$. (a) A = Co, (b) A = Ni, (c) A = Ca. Temperature-dependent X-ray diffraction patterns for $(Mn_{0.9}A_{0.1})_2V_2O_7$ with selected temperature region in cooling process (d) A = Co, (e) A = Ni, (f) $(Mn_{0.95}Ca_{0.05})_2V_2O_7$.

3.2. Temperature-dependent strain-stress loops of $(Mn_{0.9}A_{0.1})_2V_2O_7$ (A = Co, Ni, and Ca)

The measurement of strain-stress loops can reveal the ferroelectric ordering, analogous to *M-H* loops for ferromagnetic and *P-E* loops for ferroelectric ordering. It is noted from Fig. 1 that $Mn_2V_2O_7$ is in the β phase at room temperature (~300 K). In addition, the $Mn_2V_2O_7$ is extremely brittle and soft to measure the strain-stress loop. To ensure the ferroelastic transition phase in $Mn_2V_2O_7$, strain-stress loop measurements were firstly performed on Ni and Co-doped samples (x = 0.1), where $(Mn_{0.9}Co_{0.1})_2V_2O_7$ and $(Mn_{0.9}Ni_{0.1})_2V_2O_7$ are with α-phase at room temperature (see later in Figs. 3 and 4). Obviously, the strain-stress loops were observed in α-phase $(Mn_{0.9}Co_{0.1})_2V_2O_7$ and $(Mn_{0.9}Ni_{0.1})_2V_2O_7$ at room temperature shown in Fig. 2(a). These results imply that the structural, magnetic, dielectric, DSC anomalies are also associated the paraelastic (high temperature) to ferroelastic (low temperature) transition at T_S = 260–280 K. In fact, the values of the strain-stress loop on $(Mn_{0.9}Co_{0.1})_2V_2O_7$ was reproduced with higher stress using different equipment, as shown in Fig. 2(b). Further, the temperature-dependent strain-stress loops measured for $(Mn_{0.9}Co_{0.1})_2V_2O_7$, shown in Fig. 2(c)–(f), show a nonlinear strain response with increasing compressive stress, in addition to significant hysteresis with a corresponding remanent strain after unloading, demonstrating the irreversibility of the stress-induced hysteretic process. Such observations indicate the existence of a ferroelastic response in this material. The presence of remnant strain indicates that the stress-induced domain switching is irreversible. During the second cycle, a minor, closed hysteresis is also observed, which is understood to be due to the reversible motion of ferroelastic domain walls [39]. During testing, the sample was first tested at room temperature and then subsequently cooled to 0 °C, −20 °C, and then −40 °C without removal from the measurement arrangement [shown in Fig. 2 (c)–(f)]. This was done to ensure that the sample retained the same alignment throughout testing. As such, the largest remanent strain was observed during the first cycle at room temperature and subsequent loading cycles displayed a significant reduction in remanent strain. This is because of the irreversibility of the domain reorientation process, limiting the number of available domains at lower temperatures. Importantly, however, each temperature demonstrates a minor hysteresis is characteristic of ferroelastic domain wall mobility. As such, an in-depth investigation of the influence of mechanical load on the multiferroic ordering in these compositions is necessary.

3.3. Tunable structural and ferroelastic phase transition with chemical doping in $(Mn_{1-x}A_x)_2V_2O_7$ (A = Co, Ni, and Ca)

As established in Fig. 1, the $Mn_2V_2O_7$ exhibits a martensitic-like thermodynamically structural phase transition (β-α) and associated magnetization, dielectric, and DSC anomalies near to the room temperature. Furthermore, this structural transition was confirmed to be associated with the ferroelastic transition presented in Fig. 2. The tunability of the β-α phase transition temperature T_S is crucial; chemical doping is a common tool to accomplish this. Polycrystalline $(Mn_{1-x}A_x)_2V_2O_7$ (A = Co, Ni, and Ca; $0 \le x \le 0.2$) samples were successfully synthesized and characterized at room temperature, as shown in Fig. 3 (a), (b) and (c). At room temperature, $Mn_2V_2O_7$ appeared in the pure β-phase, indicating that the β-α phase transition has occurred below the room temperature. However, the structure sharply changes in Co- and Ni-doping cases even at extremely low doping concentration ($x \le 0.2$), as shown in Fig. 3(a) and (b). Therefore, Co- and Ni-doping could stabilize the α-phase at room temperature, raising the β-α phase transition towards higher temperatures. The effect of Co-doping is considerably more pronounced than that of Ni-doping. On the other hand, Ca-doping can stabilize the β-phase at room temperature, and no notable α-phase was noticed up to the doping level of $x \le 0.2$.

Additionally, synchrotron XRD was performed to further examine the temperature window of the β-α phase transition at different temperatures for x = 0.1 (Ni) and 0.05 (Ca), as shown in Fig. 3(d)–(f). Therefore, the room-temperature XRD showed a low-temperature α-phase. However, unlike Co- and Ni-doping, the β-α phase transition (maintained in β-phase) in Ca-doping did not appear in the temperature window of T = 160–240 K. Hence, the structural transition might appear at a significantly lower temperature (T < 160 K). The detailed temperature-dependent XRD data show the β-α phase transition for the other Co-, Ni-, and Ca doping levels are presented in Figs. S2 to S5 (supplementary).

3.4. DSC and dielectric properties on the structural transition of $(Mn_{1-x}A_x)_2V_2O_7$ (A = Co, Ni, and Ca)

Temperature-dependent differential scanning calorimetry (DSC)

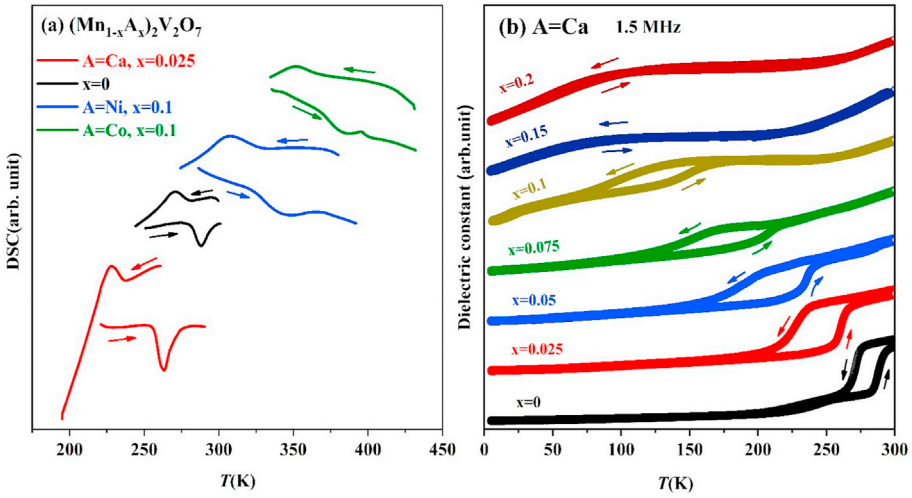

Fig. 4. (a) DSC curves of $(Mn_{1-x}A_x)_2V_2O_7$. **(b)** Ca-doping-dependent dielectric constant in $(Mn_{1-x}Ca_x)_2V_2O_7$ measured with 1.5 MHz. Both temperatures occurring the thermal hysteresis are consistent with those of structural transition in Fig. 3.

and dielectric constant measurements were performed to further explore the β-α phase transition, as shown in Fig. 4. Owing to the limitations of the temperature window of our dielectric system ($T =$ 4−320 K), we employed DSC measurements for samples with high-temperature β-α structural phase transition. By substituting Co^{2+} and Ni^{2+} at the Mn^{2+} site, both the endothermic and exothermic peaks increased at higher temperatures, as shown in Fig. 4(a). These observations are consistent with the temperature-dependent XRD results presented in Fig. 3. In Fig. 4(b), a step-like behavior was observed in the dielectric constant measurement, forming a thermal hysteresis related to the β-α phase transition. More detailed investigations on the nature of the dielectric behavior, frequency, and voltage-dependent dielectric measurements are presented in Fig. S6(a) and S6(b). The step in the dielectric measurements is insensitive for both the frequency and voltage. Moreover, the absence of pyrocurrent, shown in Fig. S6(c), at the dielectric step is reasonable because of its centrosymmetric space group, indicating that the structural transition is only a possible source for the thermo-irreversible dielectric data and is not associated with the electric polarization. As the doping level of Ca^{2+} increased, the sharp dielectric behavior became smeared, broadened, and shifted to lower temperatures, consistent with those shown in Fig. 5(e) and (f). Thermal hysteresis is not observed for $x > 0.15$, indicating that the α-phase nearly disappeared, and the structure remained in the β-phase at low temperatures.

The observations of the thermally sensitive β-α structural phase transition and associated variations in the temperature-dependent dielectric constant and DSC measurements have been noticed in many ferroelastic materials [40,41], indicating that the present β-α phase transition in $Mn_2V_2O_7$ can be attributed to the paraelastic to the ferroelastic phase transition. This is supported from the symmetry point of view. Curie symmetry principle states that the space group of the ferroelastic phase should be the subspace group of paraelastic phase [21]. The space group of low-temperature α-phase ($P\bar{1}$) is indeed a subgroup of high-temperature β-phase ($C2/m$). Moreover, the β-α phase belongs to the $2/mF\bar{1}$ crystallographic Aizu notation for ferroelastic transition [20,21]. Both experimental data and crystallographic symmetry strongly supported that the para-to ferroelastic transition accompanies β-α phase transition in $Mn_2V_2O_7$.

Finally, phase diagrams of temperature and doping dependent thermodynamic, structural β-α phase transitions, shown in Fig. 5, were constructed from Figs. 1 and 3, and Figs. S2 to S5. For the Co- and Ni-doping, β-α phase transition systematically shifts to higher temperature with an increase in the doping level. The width of the mixed-phase increased with an increasing doping level, indicating the broadness of the β-α phase transition. However, Ca-doping displays an opposite trend; the β-α phase transition shifts toward lower temperatures with an increasing Ca-doping level up to $x \leq 0.1$. For $x > 0.15$, β phase is stable down to the lowest temperature (12 K).

3.5. Theoretical interpretation on the existence of ferroelastic phase in $Mn_2V_2O_7$

Table 1 lists the total energy as the electronic states of β and α-phases obtained from the structural relaxation results using the VASP software. The β-phase can be thought of as an austenite phase that normally appears at a higher temperature, whereas the α-phase as a detwinned martensite phase that persists at lower temperature. For a shape memory alloy (SMA), the system must be heated to activate the diffusionless phase transformation process between the detwinned martensite and austenite phases. This indispensable process completes the SMA stress-strain cycle; without it, the shape memory effect or ferroelasticity cannot occur. The β-phase for Ca-doped $Mn_2V_2O_7$ was found to be 0.97336 eV, which is lower than that for the α-phase, presented in Table 1; thus, the β-phase is energetically more stable than the α-phase. However, the situation changes when the dopant is replaced by Ni or Co. For Ni- and Co-doped $Mn_2V_2O_7$, it can be seen that the α-phase is energetically more stable than the β-phase. This might be the reason for observing no ferroelasticity in Ca-doped $Mn_2V_2O_7$ in the doping range of 20%. Figs. S7 and S8 demonstrate the structural views of the relaxed structures.

Besides, two explanations are suggested for the above findings. First, the empirically measured ionic radii of Mn, Ni, Co, and Ca is 0.83 Å, 0.75 Å, 0.69 Å, and 1 Å, respectively. Because Ca has a much larger ionic size, it can generate excessive strain energy or chemical pressure that changes the Ca-doping sample's energetics and stability significantly. Second, Ca atoms belong to the alkaline earth group, whose chemical properties are much different from the 3*d* transition-metal group metals such as Mn, Ni, and Co. These theoretical expectations are in line with our experimental findings, and explain the DFT obtained energetics.

The detwinned martensite phase can be realized by taking the martensite α-phase $Mn_2V_2O_7$ from our previous study [36]. In this study, a recently developed program, namely Aimsgb [42], was used to generate the required grain (twin) boundary. Following the convention of coincidence-site lattice (CSL), the CSL grain boundary as Σ3[111]/(101) was chosen, where 3 is the number describing the ratio of the atoms in the coincidence unit cell volume to its rotated unit cell, [111] is the rotating axis, and (101) is the normal vector of the grain (twin) boundary as shown in Fig. 6(a) and (b). The strain-stress curves for twin boundaries, as presented in Fig. 6(c), were simulated as follows: stress was calculated for four five levels of strain i.e. 0.5%, 2.5%, 5%, 7.5%, and 10%. Keeping the volume of the junction as in Fig. 6(d), the structure is then relaxed and the stress for the optimal structure is calculated by VASP. The elastic moduli of the three doping cases are listed in Tables S1 and S2. The three-dimensional (3D) elastic modulus view is shown in Fig. S9 to achieve a better visualization.

Further, the twinned martensite structure was created from the α-phase using the Aimsgb program described in the preceding paragraph. Using the theoretical simulations, the crystallographically constructed Mn-hexagonal lattice at several stages can be described as a conventional strain vs. stress hysteresis loop and is displayed in Fig. 6(c). As it illustrates, the twinned boundary in α-phase relaxed with the loading of external stress and partially retained its twinned boundary when stress releases to zero resulting in the hysteresis loop. On the other hand, the α-phase converted to β-phase for $T > T_S$. According to the strain-stress curve, the detwinned and twinned martensite created two separate lines, enclosing a finite region that indicates a hysteresis loop could exist for this material (shown in Fig. 6(d)). Interestingly, red and black curves enclose a trapezoid-shaped area, which is consistent with the experimental findings (see Fig. 2). The trapezoid-shaped area strongly supports the existence of ferroelasticity in $Mn_2V_2O_7$ and offers insights into its formation.

3.6. Magnetoelastic coupling in $(Mn_{1-x}Ca_x)_2V_2O_7$

The coupling between ferroelastic and antiferromagnetic coupling in $Mn_2V_2O_7$ was investigated by applying physical pressure and chemical expansion effects on T_S and T_N to explore future applications. The temperature-dependent magnetization measurement results under physical and chemical pressures are presented in Fig. 7. Pressure is a key parameter for tuning the transition and controlling the physical properties owing to its ferroelastic nature. Indeed, the pressure effects on T_S and T_N of $Mn_2V_2O_7$ were

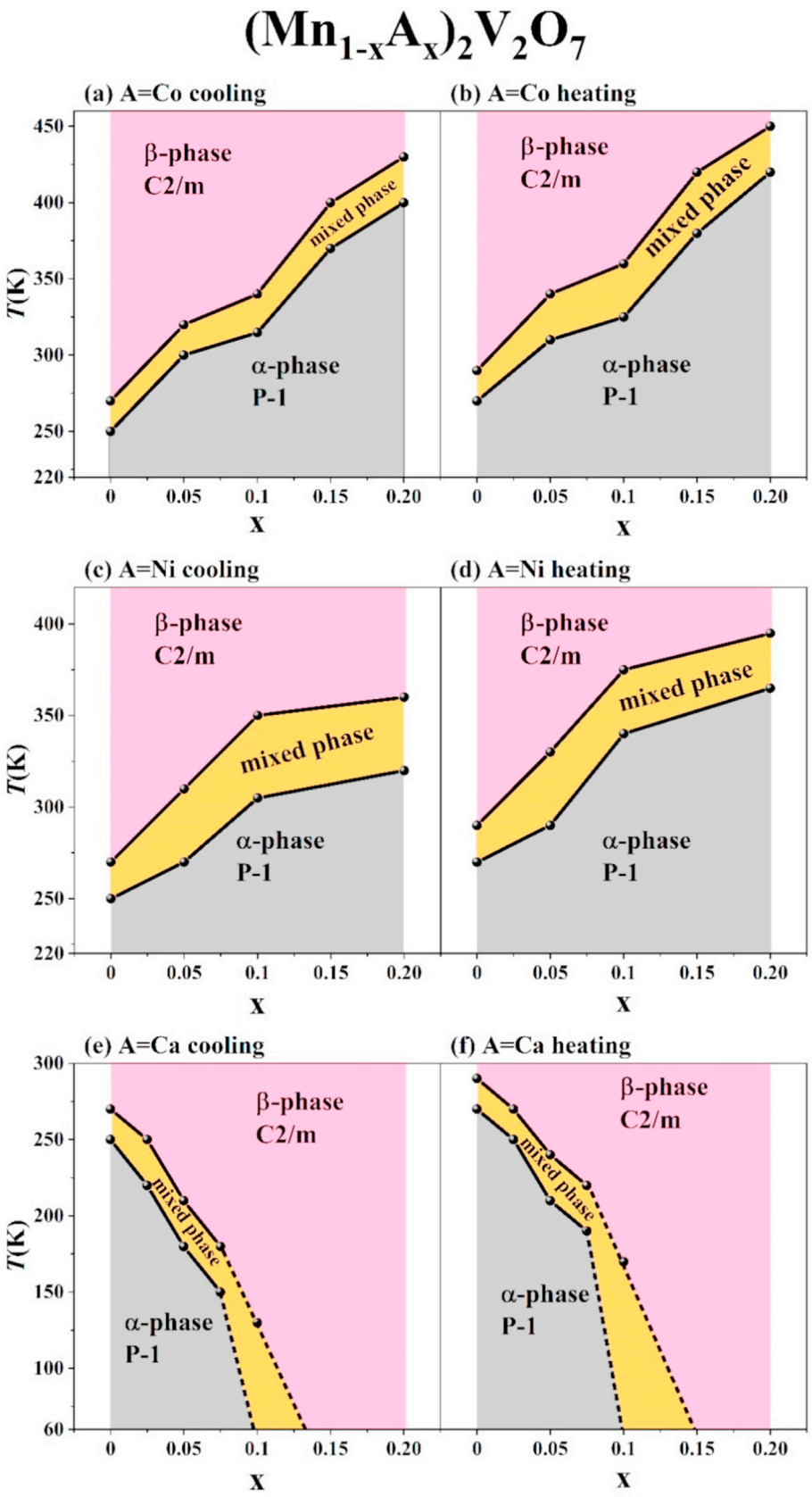

Fig. 5. Phase diagram of the structural transition in $(Mn_{1-x}A_x)_2V_2O_7$ including cooling and heating process (a, b) Co-doping, (c, d) Ni-doping, (e, f) Ca-doping. The data points were collected from Fig. 1 and Supplementary Figs. S2-S4.

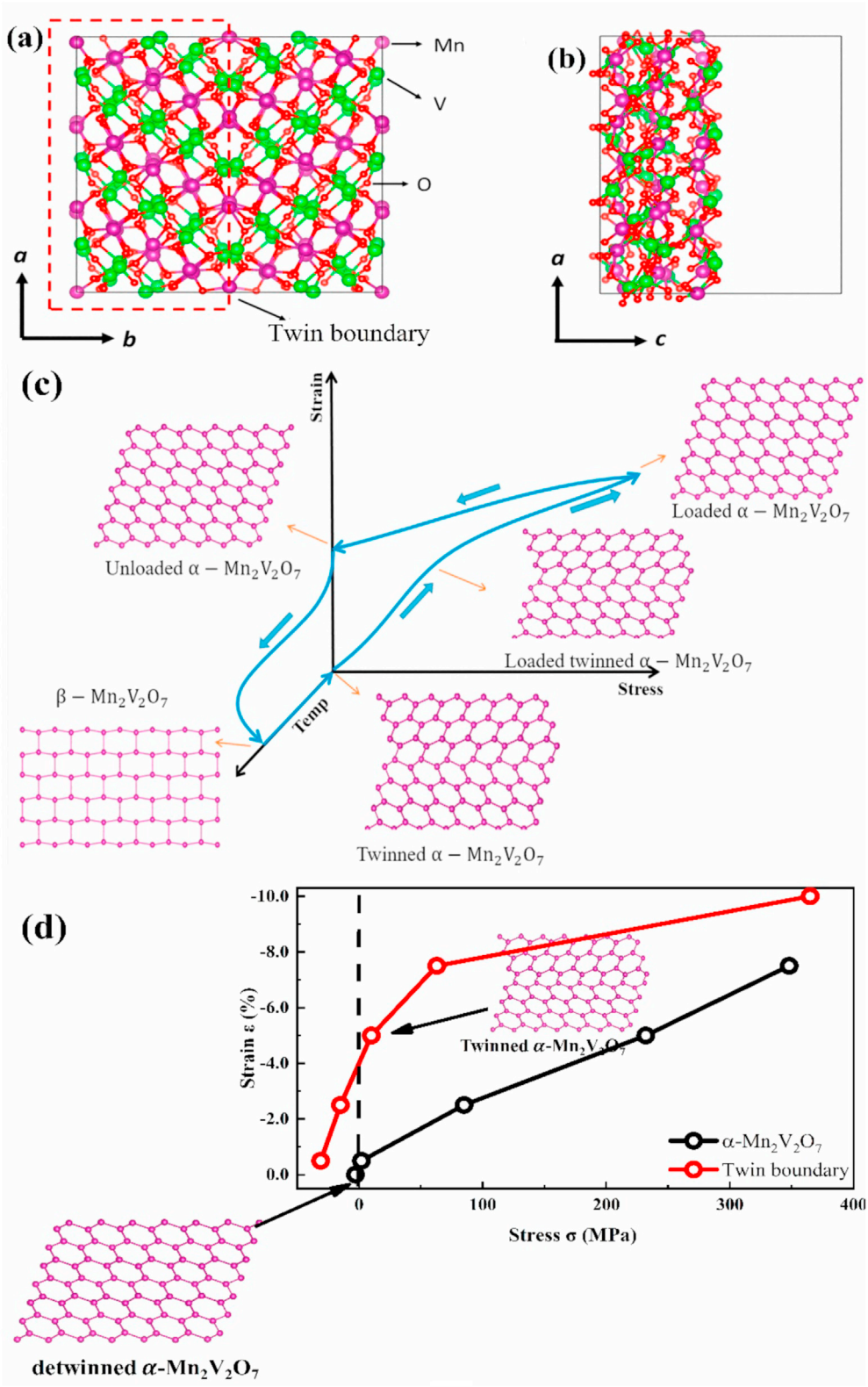

Fig. 6. (a) Created twin boundary Σ3[111]/(10 $\bar{1}$), where the CSL conventions are explained in the main text. (b) We cut half the unit cell at 1/2 $\vec{c}$ to make the cell size smaller, so to accelerate our VASP calculation. (c) Illustrate the ideal strain vs. stress loop for a typical ferroelastic system. Blue arrows indicate the stress/temperature sweeping direction; orange arrows and corresponding crystallographic pictures (theoretically simulated) denote changes in the Mn hexagonal lattice under different stress values. (d) The strain-stress curves. Stress values were extracted from VASP calculation and plotted with each prescribed strain value. The red curve denotes results with the twinned boundary. We took the relaxed structure of 0%, expanded the unit cell to each prescribed strain ratios, and performed VASP calculations, respectively to relax the structures without changing the cell shape and size to obtain the corresponding stresses.

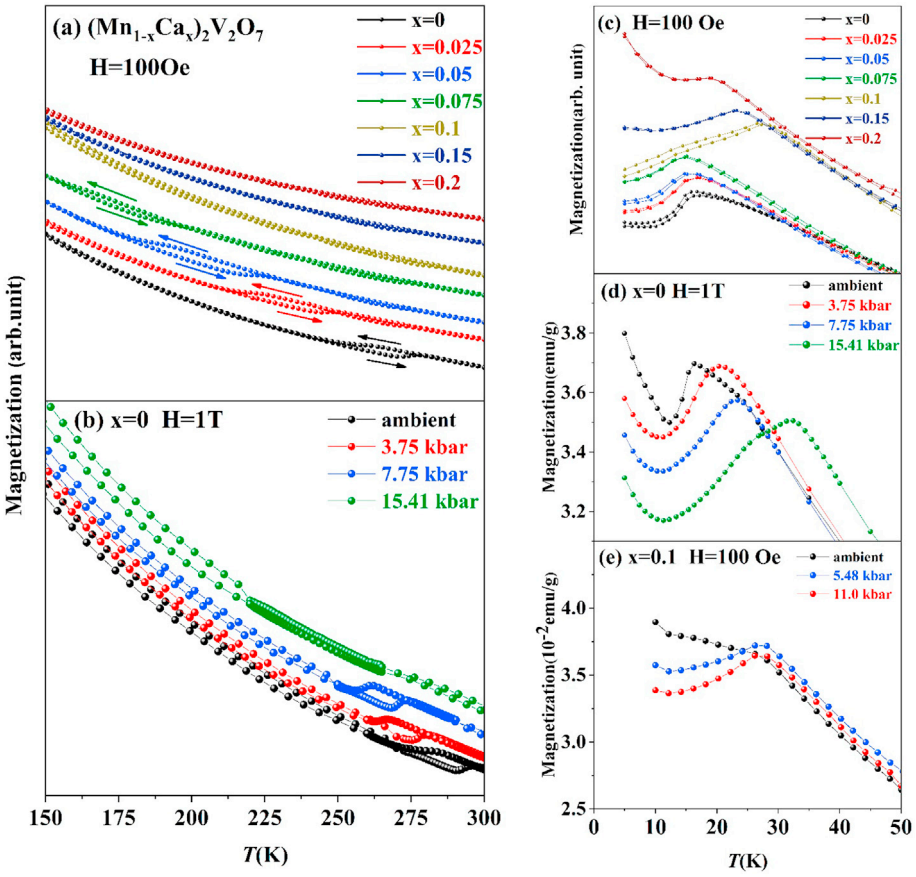

Fig. 7. Temperature-dependent magnetization of (a) (Mn1-xCax)2V2O7 ($0 \leq x \leq 0.2$) with temperature region T = 150-300 K at ambient pressure. (b) Mn2V2O7 under external pressure up to 15.41 kbar (c) (Mn1-xCax)2V2O7 ($0 \leq x \leq 0.2$) with T = 5-50 K at ambient pressure (d) Mn2V2O7 under external pressure up to 15.41 kbar, and (e) (Mn0.9Ca0.1)2V2O7 under external pressures up to 11.0 kbar. Both (b) and (d) data were taken from previous paper [23] for comparison.

partly reported [36], as shown in Fig. 7(b) and (d). At high temperatures, T_S shown in magnetization was suppressed and nearly disappeared as the external pressure increased up to 15.41 kbar, indicating that the β-phase can be stabilized by pressure; thus, it is paraelastic. Moreover, T_N was dramatically enhanced at low temperatures ($T = 17-32$ K) by pressure, indicating a strong magnetoelastic coupling between the antiferromagnetic and ferroelastic ordering. Additionally, the effects of the chemical pressure (expansion) were explored for comparison purposes. In this study, Ca^{2+} (ionic radius 1.00 Å) was used to substitute Mn^{2+} (ionic radius 0.83 Å) and to generalize the internal expansion effect in $(Mn_{1-x}Ca_x)_2V_2O_7$. Detailed variations of the lattice parameters in $(Mn_{1-x}Ca_x)_2V_2O_7$ with respect to Ca-doping level were collected from the refinement of room-temperature XRD and shown in Table S3 and Fig. S10. The lattice constants a, b, c, monoclinic angle β and unit cell volume V are monotonically and linearly changed with increasing Ca doping concentration up to 20% indicating the homogeneous substitution within this range. Since ionic radius of Ca^{2+} is larger than that of Mn^{2+}, the expansion was expected. It is noted that the a, β, and V are increased with 3.32%, 0.417%, and 2.08%, respectively, whereas b and c were slightly decreased by 0.084% and 0.932%, respectively, upon Ca doping up to 20%. Thus, this chemical Ca-doping created the anisotropic expansion effects on the structure. As shown in Fig. 7(a), the T_S was suppressed by Ca-doping, suggesting that the main phase remained in the α-phase at low temperatures when $x < 0.1$. As shown in Fig. 7(c), the $T_N \sim 17$ K was suppressed with Ca-doping up to $x = 0.075$, suddenly enhanced to approximately 27 K at $x = 0.1$, and subsequently suppressed with x up to 0.2. The sudden changes in T_N in the range of $T = 17-27$ K at $x = 0.1$ implies that the main phase of α-$Mn_2V_2O_7$ is antiferromagnetic with $T_N \sim 17$ K when $x < 0.1$, whereas that of β-$Mn_2V_2O_7$ is also antiferromagnetic at $T_N \sim 27$ K. Although T_N of the α phase was enhanced, as shown in Fig. 7(d), T_N of the β-phase was approximately unchanged by physical pressure, as shown in Fig. 7(e), indicating that the pressure is not an effective tuning parameter for T_N in the paraelastic β-phase. Therefore, the physical pressure and chemical expansion effects on T_S and T_N are anisotropic. In addition, a strong and complex coupling exists between the ferroelastic and magnetic ordering, namely magnetoelastic coupling with pressure. The *T*-x of $(Mn_{1-x}Ca_x)_2V_2O_7$ and *T*-*P* phase diagram of $Mn_2V_2O_7$ for T_S and T_N based on the data from Fig. 7 are shown in Fig. 8 for further clarification.

4. Summary

Honeycomb $Mn_2V_2O_7$ is found to undergo a para-to ferroelastic transition at $T_S = 260-280$ K using various experimental tools, such as temperature-dependent measurements in DSC, dielectric, and strain-stress hysteresis loops. This transition is coincident with the structural phase transition from the high-*T* monoclinic (*C2/m*) β-phase to the low-*T* triclinic ($P\bar{1}$) α-phase. Remarkably, the chemical doping can tune T_S of this transition, as clearly demonstrated by the temperature-dependent XRD of $(Mn_{1-x}A_x)_2V_2O_7$ (A = Co, Ni and Ca). In addition, physical pressure and chemical expansion effects were applied on $(Mn_{1-x}Ca_x)_2V_2O_7$ to correlate T_S and T_N; consequently, the magnetoelastic coupling was clearly revealed.

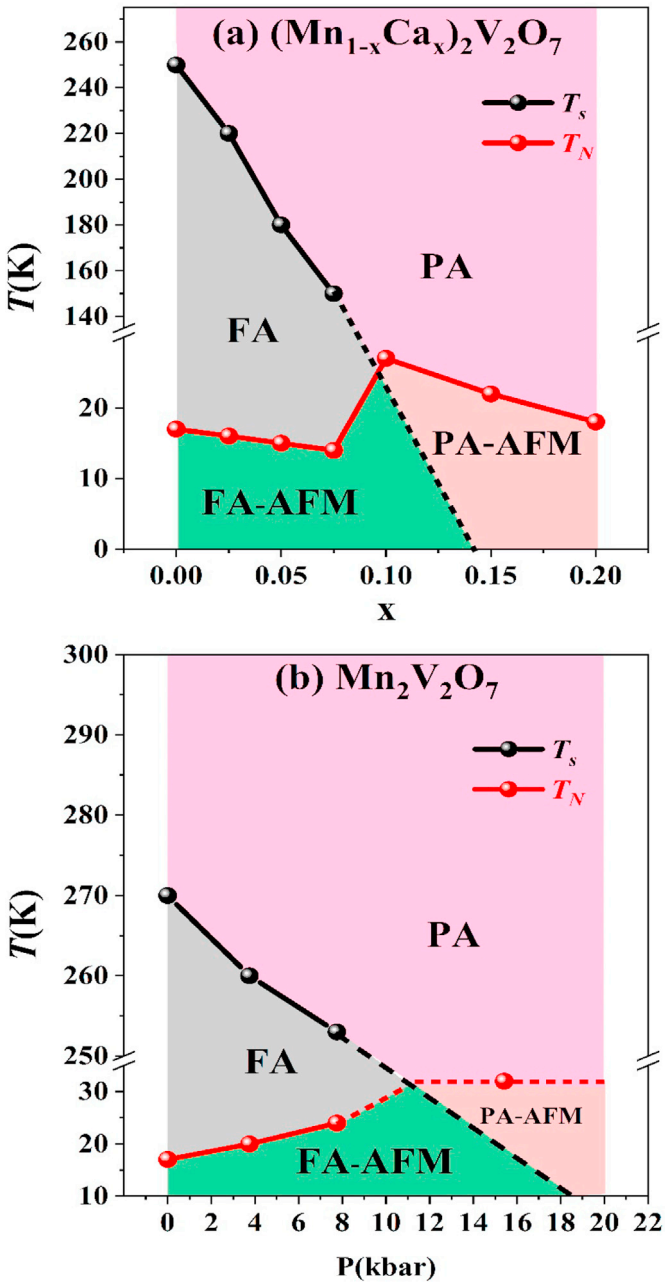

Fig. 8. Phase diagrams of (a) chemical (Ca-doping) expansion and (b) physical pressure effects on transition temperature of para-(PA) to ferro-elastic (FA) transition T_S and of antiferromagnetic (AFM) (T_N) $Mn_2V_2O_7$ were drawn from Fig. 7. For clarity, the T_S was taken only determined from the cooling temperature process of Fig. 7 (a) and (b).

Therefore, an unique type-I multiferroic material, $Mn_2V_2O_7$, with ferroelastic (T_S = 260–280 K) and antiferromagnetic (T_N = 17 K) orderings was established. The theoretical calculations supported the experimental results that the ferroelasticity would exist in the α-phase, which is more stable in Co- and Ni-doping, while β-phase becomes more stable in Ca-doping. A further and deeper understanding of the lattice or domain-wall dynamics and potential applications in $Mn_2V_2O_7$ and its related materials are highly anticipated.

Credit author statement

H. J. Chen: Methodology, Writing - Original Draft, Formal analysis, Investigation. C. H. Yeh: Investigation, Formal analysis. T. W. Kuo: Investigation, Formal analysis. D. Chandrasekhar Kakarla: Conceptualization, Investigation, Visualization, Writing - Review & Editing, Supervision, Funding acquisition, Formal analysis, Validation. H. C. Wu: Conceptualization, Formal analysis, Investigation. T. W. Yen: Software, Formal analysis, Writing - Review & Editing. S. M. Huang: Software, Data Curation, Validation. H. Chou: Investigation. M. C. Chou: Investigation. H. W. Chen: Investigation, Validation. S. W. Kuo: Investigation, Validation. Y. C. Chuang: Investigation. C. K. Chang: Investigation. U. Eckstein: Investigation. N. H. Khansur: Investigation. K. G. Webber: Supervision, Visualization, Writing - Review & Editing, Supervision, Funding acquisition. H. D. Yang: Conceptualization, Visualization, Project administration, Writing - Review & Editing, Supervision, Funding acquisition, Formal analysis.

Declaration of competing interest

The authors declare that they have no known competing financial interests or personal relationships that could have appeared to influence the work reported in this paper.

Acknowledgment

This work was supported by the Ministry of Science and Technology, Taiwan, under Grant Nos. MOST 109–2112–M–110–019, MOST 110–2923–M–110–001, MOST 108–2112–M–110–014–MY2, and MOST 110–2112–M–110–008–MY3. U. E., N. H. K. and K. G. W. gratefully acknowledge the financial support for their contributions from the Deutsche Forschungsgemeinschaft (DFG) under WE4972/2.

Appendix A. Supplementary data

Supplementary data to this article can be found online at https://doi.org/10.1016/j.mtphys.2022.100623.

References

[1] W. Eerenstein, N.D. Mathur, J.F. Scott, Multiferroic and magnetoelectric materials, Nature 442 (2006) 759.
[2] S.W. Cheong, M. Mostovoy, Multiferroics: a magnetic twist for ferroelectricity, Nat. Mater. 6 (2007) 13.
[3] N. Balke, S. Choudhury, S. Jesse, M. Huijben, Y.H. Chu, A.P. Baddorf, L.Q. Chen, R. Ramesh, S.V. Kalinin, Deterministic control of ferroelastic switching in multiferroic materials, Nat. Nanotechnol. 4 (2009) 868.
[4] H.C. Wu, K.N. Denisova, D. Menzel, D.C. Kakarla, O.V. Maximova, T.W. Kuo, Z.H. Yang, C.H. Lee, W.H. Li, H. Berger, C.W. Wang, C.K. Chang, Y.C. Chuang, J.Y. Lin, M. Gooch, C.W. Chu, A.N. Vasiliev, H.D. Yang, Antiferroelectric antiferromagnetic type-I multiferroic $Cu_9O_2(SeO_3)_4Cl_6$, Phys. Rev. B 100 (2019) 245119.
[5] N.A. Spaldin, M. Fiebig, The renaissance of magnetoelectric multiferroics, Science 309 (2005) 391.
[6] C.H. Yang, J. Seidel, S.Y. Kim, P.B. Rossen, P. Yu, M. Gajek, Y.H. Chu, L.W. Martin, M.B. Holcomb, Q. He, P. Maksymovych, N. Balke, S.V. Kalinin, A.P. Baddorf, S.R. Basu, M.L. Scullin, R. Ramesh, Electric modulation of conduction in multiferroic Ca-doped $BiFeO_3$ films, Nat. Mater. 8 (2009) 485.
[7] G. Bera, A. Surampalli, A. Mishra, P. Mal, V.R. Reddy, A. Banerjee, A. Sagdeo, P. Das, G.R. Turpu, Magnetolattice coupling, magnetic frustration, and magnetoelectric effect in the Cr-doped $FeVO_4$ multiferroic material and their correlation with structural phase transitions, Phys. Rev. B 100 (2019): 014436.
[8] Y.D. Liou, Y.Y. Chiu, R.T. Hart, C.Y. Kuo, Y.L. Huang, Y.C. Wu, R.V. Chopdekar, H.J. Liu, A. Tanaka, C.T. Chen, C.F. Chang, L.H. Tjeng, Y. Cao, V. Nagarajan, Y.H. Chu, Y.C. Chen, J.C. Yang, Deterministic optical control of room temperature multiferroicity in $BiFeO_3$ thin films, Nat. Mater. 18 (2019) 580.
[9] J.K.H. Fischer, H. Ueda, T. Kimura, Domain switching and exchange bias control by electric field in the multiferroic conical magnet Mn_2GeO_4, Phys. Rev. B 102 (2020): 054412.
[10] Y. Wang, J. Li, D. Viehland, Magnetoelectrics for magnetic sensor applications: status, challenges and perspectives, Mater. Today 17 (2014) 269.
[11] H.C. Wu, J.K. Yuan, K.D. Chandrasekhar, C.H. Lee, W.H. Li, C.W. Wang, J.M. Chen, J.Y. Lin, H. Berger, T.W. Yen, S.M. Huang, C.W. Chu, H.D. Yang, Observation of charge–transfer–driven antiferroelectricity in 3d-pyrochlore

multiferroic Cu_2OCl_2, Mater. Today Phys. 8 (2019) 34.
[12] J.F. Scott, Data storage - multiferroic memories, Nat. Mater. 6 (2007) 256.
[13] K.K. Mishra, A.A. Instan, S. Kumari, J.F. Scott, R.S. Katiyar, Lead palladium titanate: a room temperature nanoscale multiferroic thin film, Sci. Rep. UK. 10 (2020) 2991.
[14] Y.Z. Hu, L. You, B. Xu, T. Li, S.A. Morris, Y.X. Li, Y.H. Zhang, X. Wang, P.S. Lee, H.J. Fan, J.L. Wang, Ferroelastic-switching-driven large shear strain and piezoelectricity in a hybrid ferroelectric, Nat. Mater. 20 (2021) 612.
[15] C.S. Wang, X.X. Ke, J.J. Wang, R.R. Liang, Z.L. Luo, Y. Tian, D. Yi, Q.T. Zhang, J. Wang, X.F. Han, G. Van Tendeloo, L.Q. Chen, C.W. Nan, R. Ramesh, J.X. Zhang, Ferroelastic switching in a layered-perovskite thin film, Nat. Commun. 7 (2016) 10636.
[16] K.G. Webber, M. Voegler, N.H. Khansur, B. Kaeswurm, J.E. Daniels, F.H. Schader, Review of the mechanical and fracture behavior of perovskite lead-free ferroelectrics for actuator applications, Smart Mater. Struct. 26 (2017): 063001.
[17] M. Zheng, T. Usami, T. Taniyama, Shear-strain-mediated large nonvolatile tuning of ferromagnetic resonance by an electric field in multiferroic heterostructures, NPG Asia Mater. 13 (2021) 7.
[18] H. Zhang, L. Zhang, H. Luo, L. Cao, F. Li, D. Jia, H. Ke, D. Li, X. Dong, G. Liu, Y. Zhou, Dynamical electric and magnetic responses in the $Bi_{0.85}Nd_{0.15}FeO_3$ ceramic with morphotropic phase boundary, Mater, Today Phys. 21 (2021) 100559.
[19] E.K.H. Salje, Ferroelastic materials, Annu. Rev. Mater. Res. 42 (2012) 265.
[20] V. Wadhawan, Ferroelasticity, Bull. Mater. Sci. 6 (1984) 733.
[21] K. Aizu, Possible species of ferromagnetic, ferroelectric, and ferroelastic crystals, Phys. Rev. B 2 (1970) 754.
[22] X. Liu, F. Zhang, P. Long, T. Lu, H. Zeng, Y. Liu, R.L. Withers, Y. Li, Z. Yi, Anomalous photovoltaic effect in centrosymmetric ferroelastic $BiVO_4$, Adv. Mater. 30 (2018) 1801619.
[23] G. Catalan, J.F. Scott, Physics and applications of bismuth ferrite, Adv. Mater. 21 (2009) 2463.
[24] Y.-H. Seo, D.J. Franzbach, J. Koruza, A. Benčan, B. Malič, M. Kosec, J.L. Jones, K.G. Webber, Nonlinear stress-strain behavior and stress-induced phase transitions in soft $Pb(Zr_{1-x}Ti_x)O_3$ at the morphotropic phase boundary, Phys. Rev. B 87 (2013): 094116.
[25] Y.-J. Kim, H.-S. Park, C.-H. Yang, Raman imaging of ferroelastically configurable Jahn−Teller domains in $LaMnO_3$, npj Quant. Mater. 6 (2021) 62.
[26] A. Haykal, J. Fischer, W. Akhtar, J.Y. Chauleau, D. Sando, A. Finco, F. Godel, Y.A. Birkholzer, C. Carretero, N. Jaouen, M. Bibes, M. Viret, S. Fusil, V. Jacques, V. Garcia, Antiferromagnetic textures in $BiFeO_3$ controlled by strain and electric field, Nat. Commun. 11 (2020) 1704.
[27] C. Himcinschi, J. Rix, C. Röder, M. Rudolph, M.-M. Yang, D. Rafaja, J. Kortus, M. Alexe, Ferroelastic domain identification in $BiFeO_3$ crystals using Raman spectroscopy, Sci. Rep. UK. 9 (2019) 379.
[28] A. Butykai, S. Bordacs, I. Kezsmarki, V. Tsurkan, A. Loidl, J. Doring, E. Neuber, P. Milde, S.C. Kehr, L.M. Eng, Characteristics of ferroelectric-ferroelastic domains in Neel-type skyrmion host GaV_4S_8, Sci. Rep. UK. 7 (2017) 44663.
[29] S. Bhowal, J. Sannigrahi, S. Majumdar, I. Dasgupta, A comparative study of electronic, structural, and magnetic properties of alpha-, beta-, and gamma-$Cu_2V_2O_7$, Phys. Rev. B 95 (2017): 075110.
[30] R. Chen, J.F. Wang, Z.W. Ouyang, Z.Z. He, S.M. Wang, L. Lin, J.M. Liu, C.L. Lu, Y. Liu, C. Dong, C.B. Liu, Z.C. Xia, A. Matsuo, Y. Kohama, K. Kindo, Magnetic field induced ferroelectricity and half magnetization plateau in polycrystalline $R_2V_2O_7$ (R = Ni, Co), Phys. Rev. B 98 (2018) 184404.
[31] J.H. Liao, F. Leroux, C. Payen, D. Guyomard, Y. Piffard, Synthesis, structures, magnetic properties, and phase transition of manganese(II)divanadate: $Mn_2V_2O_7$, J. Solid State Chem. 121 (1996) 214.
[32] J. Sannigrahi, D.T. Adroja, R. Perry, M.J. Gutmann, V. Petricek, D. Khalyavin, Commensurate to incommensurate magnetic phase transition in honeycomb-lattice pyrovanadate $Mn_2V_2O_7$, Phys. Rev. Mater. 3 (2019) 113401.
[33] J. Sannigrahi, S. Bhowal, S. Giri, S. Majumdar, I. Dasgupta, Exchange-striction induced giant ferroelectric polarization in copper-based multiferroic material alpha-$Cu_2V_2O_7$, Phys. Rev. B 91 (2015) 220407.
[34] J. Sannigrahi, S. Giri, S. Majumdar, Magnetic and dielectric properties of $Mn_2V_2O_7$, Solid State Commun. 228 (2016) 10.
[35] Y.C. Sun, Z.W. Ouyang, Y. Xiao, Y. Su, E. Feng, Z. Fu, W.T. Jin, M. Zbiri, Z.C. Xia, J.F. Wang, G.H. Rao, Honeycomb-lattice antiferromagnet $Mn_2V_2O_7$: a temperature dependent x-ray diffraction, neutron diffraction and ESR study, Mater. Res. Express 4 (2017) 46101.
[36] H.C. Wu, D.J. Hsieh, T.W. Yen, P.J. Sun, D.C. Kakarla, J.L. Her, Y.H. Matsuda, C.K. Chang, Y.C. Lai, M. Gooch, L.Z. Deng, K.G. Webber, C.A. Lee, M.M.C. Chou, C.W. Chu, H.D. Yang, Pressure and magnetic field effects on ferroelastic and antiferromagnetic orderings in honeycomb-lattice $Mn_2V_2O_7$, Phys. Rev. B 102 (2020): 075130.
[37] K.G. Webber, E. Aulbach, T. Key, M. Marsilius, T. Granzow, J. Rödel, Temperature-dependent ferroelastic switching of soft lead zirconate titanate, Acta Mater. 57 (2009) 4614.
[38] Z.Z. He, Y. Ueda, M. Itoh, Martensitic-like transition in $Mn_2V_2O_7$ single crystals, Solid State Commun. 147 (2008) 138.
[39] D. Damjanovic, M. Demartin, Contribution of the irreversible displacement of domain walls to the piezoelectric effect in barium titanate and lead zirconate titanate ceramics, J. Condens. Matter Phys. 9 (1997) 4943.
[40] X.G. Chen, J.X. Gao, X.N. Hua, W.Q. Liao, A high-temperature molecular ferroelastic phase transition and switchable dielectric response in the trimethylbromomethylammonium salt $[C_4H_{11}NBr]$ $[PF_6]$, New J. Chem. 42 (2018) 14909.
[41] Y. Zhang, K. Awaga, H. Yoshikawa, R.G. Xiong, Ferroelastic phase transition and dielectric anomalies in 2,4,6-trimethylanilinium perchlorate, J. Mater. Chem. 22 (2012) 9841.
[42] J. Cheng, J. Luo, K. Yang, Aimsgb: an algorithm and open-source python library to generate periodic grain boundary structures, Comput. Mater. Sci. 155 (2018) 92.